MIT Libraries | DSpace@MIT

MIT Open Access Articles

Nanomechanics of organic-rich shales: the role of thermal maturity and organic matter content on texture

The MIT Faculty has made this article openly available. ***Please share*** how this access benefits you. Your story matters.

Citation: Abedi, Sara et al. "Nanomechanics of Organic-Rich Shales: The Role of Thermal Maturity and Organic Matter Content on Texture." Acta Geotechnica 11, 4 (June 2016): 775–787 © 2016 Springer-Verlag Berlin Heidelberg

As Published: http://dx.doi.org/10.1007/S11440-016-0476-2

Publisher: Springer-Verlag

Persistent URL: http://hdl.handle.net/1721.1/117472

Version: Author's final manuscript: final author's manuscript post peer review, without publisher's formatting or copy editing

Terms of use: Creative Commons Attribution-Noncommercial-Share Alike

Massachusetts Institute of Technology

Nano-Mechanics of Organic Rich Shales: The Role of Thermal Maturity and Organic Matter Content on Texture

By: Sara Abedi[1,*], Mirna Slim[2], and Franz-Josef Ulm[2]

[1] Harold Vance Department of Petroleum Engineering, Texas A&M University, College Station, TX

[2] Department of Civil and Environmental Engineering, Massachusetts Institute of Technology, Cambridge MA.

Abstract

Despite the importance of organic-rich shales, microstructural characterization and theoretical modeling of these rocks are limited due to their highly heterogeneous microstructure, complex chemistry, and multiscale mechanical properties. One of the sources of complexity in organic rich shales is the intricate interplay between micro-textural evolution and kerogen maturity. In this study, a suite of experimental and theoretical microporomechanics methods are developed to associate the mechanical properties of organic-rich shales both to their maturity level and to the organic content at micrometer- and sub-micrometer length scales. Recent results from chemomechanical characterization experiments involving grid nanoindentation and Energy Dispersive X-ray Spectroscopy (EDX) are used in new micromechanical models to isolate the effects of maturity levels and organic content from the inorganic solids. These models enable attribution of the role of organic maturity to the texture of the indented material, with immature systems exhibiting a matrix-inclusion morphology, while mature systems exhibit a polycrystal morphology. Application of these models to the interpretation of nanoindentation results on organic rich shales allows us to identify unique clay mechanical properties that are consistent with molecular simulation results for illite, and independent of the maturity of shale formation and total organic content (TOC). The results of this investigation contributes to the design of a multiscale model of the fundamental building blocks of organic-rich shales, which can be used for the design and validation of multiscale predictive poromechanics models.

Keywords: Organic-rich shale, Nanoindentation, Microporomechanics, Texture, Maturity, Organic Content

* Corresponding Author: sara.abedi@tamu.edu

1. Introduction

Over the past decade, organic-rich shales have gained significant attention in the petroleum industry. These unconventional reservoir rocks buried nearly all over the world are considered source rocks for fossil fuels. Despite the importance of organic-rich shales, microstructural characterization and theoretical modeling of these rocks are limited due to their highly heterogeneous microstructure, complex geochemistry, and multiscale mechanical properties.

One of the sources of complexity in organic-rich shales is the intricate interplay between micro-texture evolution and kerogen maturity [1, 18, 20, 23, 24]. There is increasing evidence that the maturation of organic matter changes the micro-texture of organic-rich shales [18-20, 23, 25] contributing to the changes in mechanical properties of the rock. Recent findings of Prasad et al. [2009a,b] and Zargari et al. [2013] show that the texture of organic-rich shales undergoes major transformation as maturity increases with immature shales exhibiting a more connected texture compared to mature shales. Incorporating this micro-textural evolution into micromechanical models of organic rich shales is a key in multiscale modeling of such complex materials.

The overall goal of this work is to relate organic maturity and total organic content (TOC) to the effective mechanical properties of the clay/kerogen phase in organic-rich shales using the experimental results of a coupled energy dispersive x-ray spectroscopy (EDX)-nanoindentation technique. The technique consists of assessing mechanical and chemical properties at micrometer and sub-micrometer length scales using grid nanoindentation and EDX techniques to isolate various material phases of interest (e.g. clay-rich phase). Herein, with a view on the micromechanical modeling of organic-rich shales, a texture hypothesis is tested. The hypothesis consists of attributing the first-order contribution of organic maturity on composite response of immature and mature systems to a texture effect, by considering a matrix-inclusion morphology for immature systems and a polycrystal/granular morphology for mature systems – while recognizing that the reality of such highly heterogeneous material systems like source rocks is somewhat situated in between. The successful implementation of these models to interpret nanoindentation results from various organic-rich shales allows us to identify unique mechanical properties of clay that are insensitive to maturity and TOC of the organic matter in shale formation; as well as consistent with molecular simulation results of illite [13] and back-analysis results from acoustic measurements [15]. The information gathered at these fundamental scales are pivotal for designing and validating predictive upscaling models.

To explore our hypothesis, the investigation employs a multiscale structure thought model of organic-rich shales, shown in Figure 1. The three-level model spans the scales from the elementary building blocks (clay minerals in case of clay-dominated formations) of organic-rich shales (level 0) to the macroscopic inorganic/organic hard inclusion composite (level II). The different length scales considered in the three-level thought model satisfy the scale separability condition for the application of micromechanics models; that is, the characteristic length scale of each level is much smaller than the characteristic length scale of the next level. For instance, Level II represents the millimeter and sub-millimeter ranges, a scale at which the material is a porous clay/kerogen composite intermixed with silt-sized inclusions (e.g., quartz, calcite, pyrite, etc.). In turn, Level I represents the sub-micrometer range, a scale at which nanoindentation and advanced observational methods such as SEM and EDX are applied. Finally, Level 0 is the scale of the elementary clay particles at nanometer length scales, which have been recently addressed by means of molecular simulations [9, 13].

The paper is organized as follows: Section 2 summarizes the studied materials and presents an overview of the experimental procedure and micromechanical model used as a means for hypothesis testing and back-analysis of the experimental results. The results from back-analysis algorithm performed on various shale samples that varied in maturities and organic contents are then presented in Section 3. Finally, in Section 4, the outcomes are discussed in light of various computational and experimental results.

2. Materials and Methods

2.1. Materials

Several organic-rich shale samples of different mineralogy and maturity levels are considered: Haynesville; Marcellus; Fayetteville; Antrim; and Barnett. The samples used in this study are the same samples as those studied in Abedi et al. [2016]. Experimental information regarding mineralogy, TOC, and porosity of the considered samples are summarized in Table 1. The mineralogy and TOC data were obtained by x-ray diffraction and Rock-Eval pyrolysis, respectively. Illite and mixed illite-smectite are the most common clay minerals found in these samples with relatively smaller amounts of kaolinite and chlorite. The porosity of the samples was either obtained using Gas Research Institute (GRI) protocols (Haynesville), or calculated employing bulk densities and mineralogy information. For nanoindentation and EDX experiments, all samples were prepared following the procedure described in Abedi et al. [2016].

For the purpose of developing multiscale micromechanics models for organic-rich shales, the information regarding mineralogy and porosity for all studied samples are converted into corresponding volumetric parameters. Such quantities become important, particularly in modeling mechanical behavior of the samples, as they weigh the contribution of the relevant phases in the mechanical response of the material. Based on the multi-scale structure thought model for organic-rich shales described in Section 1, the volume fraction of the i^{th} mineral in the sample at the macroscopic scale (level II) is obtained from:

$$f^i = (1-\phi^{II})\frac{m_i/\rho_i}{\sum_{k=1}^{N}\left(m_k/\rho_k\right)} \tag{1}$$

$$\sum_{k=1}^{N} f^i + \phi^{II} = 1 \tag{2}$$

where N denotes the number of material phases (including kerogen) in the sample, m_i stands for the mass fraction provided by, e.g., X-Ray Diffraction (XRD), and ρ_i represents the corresponding mass density; whereas ϕ^{II} is the measured porosity. Densities of 2.65 ~ 2.82, 2.65, and 2.71 [g/cm^3] are considered for clay (depending on type of clay), quartz and calcite, respectively. A variety of values have been used in the literature for the density of organic matter, most of which fall within a narrow range. For instance, Okiongbo et al. [2005] obtained density values of kerogen in the range 1.18-1.35 g/cc depending on the maturity and phase of petroleum generation. Mavko et al., [2009] reported a range of 1.1-1.4 g/cc, whereas Vernik and Landis [1996] used a value of 1.25 g/cc in their calculations. Taking into account these values, a kerogen density of 1.2 g/cc is assumed in this study. The sensitivity of our

results with regard to this assumption is later on discussed as well.

Table 2 summarizes the thus obtained volume fractions of the detected material phases in the samples. Maturity levels of investigated samples were assessed by RockEval analysis [10]. The aforementioned method characterizes the Haynesville, Marcellus, and Fayetteville samples as mature gas shale samples, while the Barnett and Antrim samples were categorized to be immature.

2.2. Chemomechanical Characterization

The focus of our study will be the porous kerogen/clay phase in the samples that were isolated by means of a coupled nanoindetation and Energy dispersive x-ray spectroscopy technique developed in detail in Abedi et al. [2016] for the considered samples. The technique which extends earlier work by Ulm and co-workers [29, 30] for shales and other heterogeneous materials to organic-rich shale samples consists of assessing mechanical and chemical properties at micrometer and sub-micrometer length scales by clustering grid nanoindentation results and Energy dispersive x-ray spectroscopy results for phase identification. Specifically, the grid nanoindentation experiment consists of carrying out indentation experiments on a regular grid of an exposed sample surface. At each grid point an indenter tip of known geometry and mechanical properties is pushed onto the surface of the material of interest [3, 31]. The mechanical properties of the indented material (indentation modulus, M, and hardness, H) are then obtained from the response of the material during indentation test:

$$M = \frac{\sqrt{\pi}}{2}\frac{S}{\sqrt{A_c}} \tag{3}$$

$$H = \frac{P}{A_c} \tag{4}$$

where $S = dP/dh$ is the measured initial slope of the unloading branch of the P-h curve, A_c is the projected area of contact between the indenter tip and sample surface, and P is the measured maximum indentation load.

In an attempt to couple this mechanical response with the chemical make-up of the indented material volumes, energy dispersive x-ray spectroscopy (EDX) maps are collected over the pre-conducted nanoindentation grids. The EDX technique utilizes the x-Ray spectrum emitted from the incited solid specimen as a result of a beam of electrons bombarding the sample surface to provide a localized chemical analysis. The emitted x-rays are then classified based on their energy.

The results of nanoindentation and EDX are coupled by averaging EDX elemental intensities over 2 μm diameter area centered at each indentation point and then by feeding mechanical and chemical data into clustering analysis [1]. Through such clustering analysis, one can identify the most likely number of clusters in a data set as well as the uncertainty of observations belonging to a cluster based on statistical criteria. Depending on the material phase of interest, different elemental intensities required for proper phase identification are incorporated into statistical analysis. For the investigated samples in this study, in order to identify clay-rich phases, maps of “Si” and “Al” from EDX were used [1]. The coupled indentation-EDX clustering technique thus provides a means of isolating among the organic and inorganic phases in shale, a distinct porous kerogen-clay mixture phase at a length scale of 1-4 μm. This length scale is defined in indentation tests by the indentation depth, as an indentation test carried out to

an indentation depth of h, probes roughly the material response of a volume 3-4 times the indentation depth. In EDX, this length scale is defined by the excitation voltage. In the coupled indentation-EDX technique, the two length scales are chosen to coincide. Details are discussed in Abedi et al. [2016], and Refs. [29, 30].

2.3. Micromechanichhal Models: Back-Analysis of Particle Properties, Kerogen Volume Fractions, and Packing Density Distributions

With a focus on the thus identified porous kerogen/clay phase in the samples, we employ micromechanics model to identify the role of TOC and maturity on the homogeneous indentation response (M,H) of the porous kerogen/clay phase in different shale formations. Micromechanical models provide a tool to infer mechanical properties and microstructure of the solid forming the porous phase from indentation results [21]. In an organic-rich shale, the indentation volume probed by a Berkovich indenter is composed of a cohesive inorganic phase, organic phase, and an empty pore space. In order to satisfy the scale separability condition, the characteristic pore throat radii are assumed to be much smaller than the indentation depth, h (Figure 2). Therefore, the mechanical response in an indentation test, i.e., indentation modulus (M) and indentation hardness (H), are representative of the homogenized response of the composite porous organic/inorganic material. The homogenized response of the material can be written in a dimensionless form as [21]:

$$\frac{M}{m_s} = \Pi_M \left(\frac{C_{ijkl}}{m_s}, \eta_s, \eta_k, \eta_0 \right) \tag{5}$$

$$\frac{H}{h_s} = \Pi_H (\eta_s, \eta_k, \eta_0) \tag{6}$$

The above expressions indicate that the homogenized response of the material depends on the asymptotic inorganic solid properties, $m_s = lim_{\eta_s \to 1} M$ and $h_s = lim_{\eta_s \to 1} H$; the inorganic solid fraction or packing density of the inorganic phase, η_s; the volume fraction of the organic phase, η_k; and the percolation threshold, η_0, which characterizes the microstructural morphology. The implementation of dimensionless expressions (5) and (6) is based on the following assumptions: (1) there exists an inorganic phase along with an organic phase at each indentation point; (2) the difference from one indentation point to another is the volume fraction of the inorganic phase; and (3) the mechanical properties of organic matter (modulus and hardness) are negligible compared to the inorganic solid phase.

Much of our modeling approach developed below is based on hypothesis testing using micromechanical models. Given considerations of diagenesis, the hypothesis testing approach is summarized as follows: We assume that mature and immature source rocks do differ in first approximation in terms of a (mechanically) ‘effective’ morphology. Specifically:

- Immature samples are assumed to exhibit a matrix-inclusion morphology (or Mori-Tanaka morphology), [16, 2] with percolation threshold $\eta_0 = 0$, thus representing a continuous microstructure weaved together by organic matter.

- Mature samples are assumed to follow a polycrystal or granular morphology (or self-consistent scheme with percolation threshold $\eta_0 = 0.5$), with no phase (organic or inorganic) playing a dominant role as matrix.

In both of the developed models, particle shape is assumed to be isotropic (i.e., spherical shape); with all the anisotropy at level 0 resulting from the intrinsic transverse isotropy of the elementary building block. This assumption is based on the fact that aspect ratios and particles orientation do not appear to have a first-order impact on the effective mechanical properties of porous rocks with high packing density of grains (see Refs. [17, 32, Figure 2]).

The hypothesis of attributing different textures to immature and mature formations is consistent with recent findings by Prasad et al. [18-20] where a mesotextural evolution of organic rich shales as a function of maturity was shown. To test our hypothesis, we refer to linear micromechanics theory for elastic composite properties, and to non-linear micromechanics theory for strength properties in terms of hardness [3].

2.3.1. Linear Homogenization of Elasticity Properties

Linear micromechanics theory provides a means to determine the homogenized stiffness tensor of the anisotropic porous organic/inorganic composite from [6-8, 17, 14]:

$$\mathbb{C}^{hom} = \sum_r \eta^r \mathbb{C}^r \mathbb{A}^r \tag{7}$$

The homogenized (drained) stiffness tensor $\mathbb{C}^{hom}$ depends on the stiffness $\mathbb{C}^{\mathrm{r}}$, packing density η^r, and the so-called strain concentration tensor $\mathbb{A}^{\mathrm{r}}$ of each phase, given by [22, 7, 17, 14]:

$$\mathbb{A}^r = [\mathbb{I} + \mathbb{P}^r : (\mathbb{C}^r - \mathbb{C}^0)]^{-1} : \left\{\sum_s \eta_s [\mathbb{I} + \mathbb{P}^s : (\mathbb{C}^s - \mathbb{C}^0)]^{-1}\right\}^{-1} \tag{8}$$

where $\mathbb{I}$ is the fourth-order unit tensor, while $\mathbb{P}^s$ is the Hill tensor that characterizes particle interactions, particle shape, etc. For the Mori-Tanaka morphology (applied for immature samples, Figure 2b) in which the matrix plays the prominent morphological role, $\mathbb{C}^0 = \mathbb{C}^{\mathrm{mat}}$, with $\mathbb{C}^{\mathrm{mat}}$ being the stiffness of the matrix phase. In case of a self-consistent estimate (granular morphology for mature samples, Figure 2a) in which none of the phases play the role of the matrix, $\mathbb{C}^0 = \mathbb{C}^{\mathrm{hom}}$, where $\mathbb{C}^{\mathrm{hom}}$ is the homogenized stiffness of the composite material. For comparison with experimental data (forward and backward analysis), the values of the stiffness tensor can be compressed into equivalent indentation moduli for transversely isotropic material M_1 (indentation into the bedding plane, i.e., normal to the axis of material symmetry, X1, and X2) and M_3 (in the direction of material symmetry, i.e., normal to bedding, X3) [5]:

$$M_3 = 2\sqrt{\frac{C_{11}C_{33} - C_{13}^2}{C_{11}}\left(\frac{1}{C_{44}} + \frac{2}{\sqrt{C_{11}C_{33}} + C_{13}}\right)^{-1}} \tag{9}$$

$$M_1 \approx \sqrt{\sqrt{\frac{C_{11}}{C_{33}}}\frac{C_{11}^2 - C_{12}^2}{C_{11}} M_3} \tag{10}$$

Figure 3 displays the resulting continuous functions of normalized indentation modulus $\frac{M}{m_s}$ determined from equations (7)-(10) versus packing density of porous organic/inorganic composite (orange curve), considering a granular (Figure 2a) and a Mori-Tanaka (Figure 2b) morphology for mature and immature samples, respectively. For the purpose of comparison and to illustrate the effect of adding organic matter to the porous inorganic composite, the results of porous inorganic phase are also shown in Figure 3 (blue curve). The horizontal shift between orange and blue curves represents the volume fraction of the organic matter. This shift is due to the negligible stiffness and hardness of kerogen compared to that of clay.

2.3.2. Non-Linear Strength Homogenization

Based on nonlinear micromechanics [7, 11-12], a scaling relation of the form $H = h_s \times \Pi_H$ is obtained for a cohesive solid that obeys Von-Mises strength criterion, with h_s representing the solid's hardness which relates to the solid's cohesion c_s by

$$h_s = a c_s \tag{11}$$

With the dimensionless expression for hardness in Eq. (6) and for the case of granular morphology (self-consistent scheme) applicable to mature samples, the dimensionless expression Π_H reads as [3]:

$$\Pi_H = \frac{\sqrt{2\left(1 - 2(\varphi + \eta_k)\right)} - \left(1 - 2(\varphi + \eta_k)\right)}{\sqrt{2} - 1}\left(1 + b(\varphi + \eta_k) + c(\varphi + \eta_k)^2 + d(\varphi + \eta_k)^3\right) \tag{12}$$

whereas for the Mori-Tanaka morphology applicable to immature samples:

$$\Pi_H = (1 - \varphi - \eta_k)\left(1 + e(\varphi + \eta_k) + f(\varphi + \eta_k)^2 + g(\varphi + \eta_k)(1 - \varphi - \eta_k)^3\right) \tag{13}$$

with the following fitted parameters [12]:

$\mathrm{a} = 4.7644, \mathrm{b} = -5.3678, \mathrm{c} = 12.1933, \mathrm{d} = -10.3071, \mathrm{e} = -1.2078, \mathrm{f} = 0.4907,$ and $\mathrm{g} = -1.7257$. It should be noted that in contrast to the stiffness model, the strength-hardness scaling relations here above are based on the assumption of strength isotropy of the elementary particles and microtexture, described by the cohesion c_s only. This assumption needs to be verified when applying to real materials in the course of this investigation. Figure 4 illustrates the scaling of the hardness with the packing density, and specifically shows the influence of kerogen content as a shift of the percolation threshold.

It should be emphasized that the model thus defined considers kerogen's strength and stiffness negligible compared to the inorganic solid particles properties. This assumption defines the limits of the model, which should not be used for predictive purposes for samples that exhibit packing densities close to the percolation threshold. Fortunately, given the typically extremely low porosity of organic-rich shales –compared to other sedimentary rocks (sandstone, limestone)–, this restriction is not relevant for the application of these models in this investigation.

2.3.3. Back-Analysis Algorithm

The above scaling relations between porosity, kerogen volume fraction, cohesion, indentation modulus, and hardness form the backbone of our inverse approach to obtain mechanical properties of the inorganic solid phase from indentation data (reminding ourselves that the approach neglects strength and stiffness properties of kerogen, making the inorganic properties the sole mechanical unknowns of the problem). More specifically, the micromechanics models are employed in an inverse approach to infer from the gathered experimental mechanical information (M,H) of the porous organic/inorganic composite at level I, the mechanical properties of the inorganic solid phase, volume fraction of kerogen, and porosity distribution of organic/inorganic mixture phase at level 0.

Following our hypothesis testing approach (Section 2.3), in the case of mature samples, for which we consider a granular (self-consistent) morphology, two hypotheses are proposed: 1) the porosity is self-consistent, i.e., the porosity is distributed evenly in all phases of the material; and 2) the organic matter is mainly concentrated in the clay phase (see Refs. [33-35]). In the case of immature samples, for which we consider a matrix-inclusion morphology, the hypothesis is that the clay phase plays the role of the matrix and porosity and kerogen are concentrated in this matrix.

More specifically, the porous kerogen/clay phase assessed by nanoindentation is composed of the inorganic solid phase (clay), the organic phase (kerogen), and pore space; that is, in terms of volume fractions:

$$\eta_s + \eta_k + \varphi^I = 1 \tag{14}$$

where φ^I is the porosity at level I. The assumed porosity distribution allows us to distinguish:

- For the granular morphology (applicable to mature systems), the assumed self-consistent porosity distribution implies that porosity is distributed evenly in all phases of the material; i.e., $\varphi^I = \phi^{II}$ (porosity at level I or mesoscale is equivalent to the porosity at level II). The kerogen volume fraction at level I is then obtained from:

$$\eta_k = \frac{f_k}{f_k + f_c + \phi^{II}_{k+c}} \tag{15}$$

  where f_c and f_k are volume fractions of clay and kerogen at level II respectively (section 2.1) and ϕ^{II}_{k+c} is the portion of ϕ^{II} which belongs to clay and kerogen phase.

- For the Mori-Tanaka morphology applicable to immature samples, in which we consider that both porosity and kerogen are (mainly) concentrated in the clay phase (the matrix), kerogen volume fraction and porosity at level I are obtained from:

$$\eta_k = \frac{f_k}{f_k + f_c + \phi^{II}} \tag{16}$$

$$\varphi^I = \frac{\phi^{II}}{f_k + f_c + \phi^{II}} \tag{17}$$

Table 3 summarizes the volume fraction of kerogen at level I obtained from Eqn. (15) and (16) for all mature samples under study. Porosity at level I for immature samples (Barnett and Antrim) are reported in Table 4.

The inverse analysis algorithm, also referred to as back-analysis, is formulated with the constraint of having the average porosity within the clay phase of one indentation grid equal to the porosity obtained experimentally for the sample under study. Therefore, in this approach, the unknowns of the problem are the inorganic solid phase properties (the inorganic solid phase properties are assumed to be constant over the indentation grid), m_s (1 or 3), c_s, kerogen volume fraction η_k, and the local porosity φ_i, for N indentation points, resulting in N+3 unknowns. Indentation test results, M_i and H_i, and the average porosity in the clay/kerogen phase (obtained by following the aforementioned process) are known, giving a total of 2N+1 known properties. Therefore, for a large number of indentation data, the system of equations becomes highly over-determined and an estimation of unknown properties should be feasible.

The inverse analysis algorithm is implemented as an optimization algorithm which generates the optimum properties of the inorganic solid phase, volume fraction of kerogen, and local porosities, which result in minimum differences between indentation results and model predictions.

Figure 5 shows the typical outcome of the back-analysis. Indentation modulus, M, and indentation hardness, H, are plotted versus the solid packing density (clay + kerogen) estimated for each individual indentation point in a single nanoindentation grid. The results demonstrate the highly heterogeneous nature of the studied materials even within one phase (clay/kerogen phase in Haynesville samples in Figure 5).

2.4. Statistical Analysis of Indentation Data

The continuum micromechanics models employed in this study rely on the principle of ergodicity, meaning that, the spatial average estimated over a sufficiently large sample is representative of mean value over random fluctuations stemming from the underlying heterogeneity. Since organic-rich shales are highly heterogeneous materials in terms of mineralogy and texture and in order to check the sensitivity of the back-analysis approach with respect to the number of indents fed into the algorithm, a statistical analysis is performed in which various combinations of indentation tests from a pool of 928 indents all within the same sample (e.g., Marcellus), were randomly selected for the back-analysis.

To estimate the error introduced in the results when analyzing samples with small data points, and to recommend a minimum sample size to work with when analyzing the clay/kerogen phase, we assume that the back-analysis of the whole population gives the "real" value of the solid properties. Large standard deviations (Fig. 6a) predict large errors (Fig. 6b) especially when working with sample size n<500. The results suggest the need for at least 500 independent indentation tests in the clay matrix to

capture its heterogeneity and to have less than 10% errors calculating the clay solid properties. Errors up to 15% should be expected when back-analyzing individual grids consisting of 100-200 indents in the clay phase.

A sensitivity analysis was also performed to investigate the quality of back-analysis results given uncertainty in the model constraint that is imposed (e.g., average porosity). In summary, in case of mature samples with assumed granular morphology, a 10% increase in the average porosity results in approximately 1.5% reduction in m_s, 0.07% reduction in h_s, and 1.4% reduction in estimated volume fraction of kerogen. In the case of immature samples with assumed matrix-inclusion morphology, the same 10% increase in average porosity entails a 6.9% decrease in m_s, 0.2% decrease in h_s, and 4.9% lower volume fraction of kerogen. The low sensitivity of the model with respect to the imposed constraint is indicative of the reliability of the algorithm, hence confirming the robustness of the model itself.

The present modeling effort represents a first attempt to test our hypothesis regarding textural effect of maturity and distribution of porosity and organic matter within different phases in organic rich shales. In the next two sections, the results from applying the model to various shale samples described in section 2.1 are presented and discussed.

3. Results

Nanoindentation grids in orthogonal directions were performed on organic-rich shale samples described in Section 2.1. Using the coupled EDX-nanoindentation clustering technique (see Section 2.2), we identified the clay-rich phases in the samples, by considering in the clustering algorithm the elemental intensities of "Si" and "Al" at each indentation point, together with the mechanical data, *M* and *H*.

The mechanical indentation data of each clay/kerogen phase was fed into the back-analysis algorithm (Section 2.3.3) to estimate the mechanical properties of the inorganic solid phase, the kerogen volume fraction, and the porosity distribution within the indentation grids.

Figure 7 displays the clay indentation modulus obtained from the back-analysis of indentation results versus (a) volume fraction of kerogen and (b) volume fraction of clay ($\eta_c = 1 - \eta_k - \varphi$). In obtaining volume fraction of kerogen, the TOC values reported in Section 2.3.3 were used considering that kerogen is mainly concentrated in the clay phase while assuming a kerogen density of 1.2 g/cm^3 for all samples. The results show a very consistent range of values for stiffness in X1 and X3 directions (shaded areas) independent of the maturity level and the amount of organic matter in the samples. This demonstrates the successful separation of the effect of organic matter from the inorganic phase (clay particles). The resulting clay stiffness values are M_1 =63.1 ± 8 GPa and M_3 =48.5 ± 9.2 GPa in X1 and X3 directions, respectively. The results of the t-test show that the difference between the clay indentation modulus in X1 and X3 directions is statistically significant, indicating anisotropy in elasticity (P=5×10^{-7}, at the 5% significance level).

Figure 8 shows the clay hardness versus (a) volume fraction of kerogen and (b) volume fraction of clay. The shaded areas represent the overlapping range of values obtained for clay hardness in X1 and X3 directions, which are H_1 =2.6 ± 0.6 GPa and H_3 =2.2 ± 0.8 GPa, respectively. Despite increased amount of scatter in the obtained solid hardness values, the resulting clay hardness is independent of the maturity level and the amount of organic matter in the samples. In contrast to stiffness, however, from a

statistical perspective, the t-test indicates an isotropic strength-hardness behavior of the clay particles (P=0.07, at the 5% significance level). This isotropy a posteriori confirms the model assumption of the hardness-strength model herein employed (Section 2.3.2) based on the assumption of an isotropic strength behavior of the elementary components.

Figure 9 graphically evaluates the results of the back-analysis by comparing the volume fraction of kerogen as predicted by the model with the ones obtained from TOC measurements. The performance of the model regarding the prediction of kerogen volume fraction from indentation data is satisfactory especially for Haynesville samples, Marcellus samples with low amount of TOC, and the immature samples. However, the model under-predicts kerogen volume fraction in the Marcellus samples with high amount of TOC and in the Fayetteville samples. There are several parameters that might contribute to the deviation of model predictions from TOC measurements, but the most likely is the variability in kerogen density. In our analysis, this density was assumed to be constant and equal to 1.2 g/cm^3 for all samples, while it may well vary depending on its chemical composition and maturity level. Since kerogen density is not an input in our analysis, it hardly changes the model predictions (clay indentation modulus, hardness and predicted kerogen volume fraction). However, it changes the calculated volume fraction of kerogen at level I obtained from TOC measurements (equations 15-16). Based on our analysis, a 10% increase in kerogen density results in a 6-9% reduction in calculated kerogen volume fraction at level I for both mature and immature samples. Furthermore, the presented results are based on measurements performed on approximately 100 x 100 μm^2 areas whereas TOC values are obtained at the macroscale representing the average properties of the material. Therefore, a refined approach should consider the local variability of kerogen density and thus volume fraction. Finally, some fluctuations observed in the results might be due to the fact that the complex morphology of these shales is somewhat situated in between the two considered asymptotic morphologies: granular for mature, matrix-inclusion for immature. Otherwise said, a more refined approach that considers morphologies between these two asymptotes (while incorporating other microstructural elements such as shape and statistical distribution of different phases) could potentially reduce the fluctuations and thus improve the accuracy for predictive purposes. This goes beyond the purpose of this investigation and its focus on first-order effects of maturity on texture.

4. Discussion

The coupled chemo-mechanical approach developed in this research permits to effectively separate, through micromechanics modeling, clay particle properties from kerogen. Herein, the micromechanics models are tools for testing our hypothesis that the effect of maturity on measurable properties can be captured by different textures, ranging from matrix-inclusion morphology for immature systems to a polycrystal morphology for mature systems. The discussion below is dedicated to reviewing the obtained results.

4.1. Model Validation at Level I

The indentation modulus and hardness of the porous clay/kerogen composite of the studied shale samples are compared to the clay packing density (which is $\eta_c = 1 - \eta_k - \varphi$) in Figures 10 and 11. For ease of comparison, the results of indentation in X1 and X3 directions are divided into two groups: mature and immature samples.

As a means for hypothesis testing and for the comparison with indentation results, the model predictions of $M_1(\eta_c)$, $M_3(\eta_c)$, and $H(\eta_c)$ for both granular and matrix-inclusion morphologies are displayed in

Figures 10 and 11. The bold curves represent model curves in X1 direction and the thinner ones are corresponding curves in X3 direction.

In obtaining model curves, we consider the following set of solid clay particle properties that correspond to the asymptotic case $\eta_c \to 1$: $M_{1,\eta_c\to 1} = 63.1$ GPa , $M_{3,\eta_c\to 1} = 48.5$ GPa, and $H_{1,\eta_c\to 1} = 2.6$ GPa and $H_{3,\eta_c\to 1} = 2.2$ GPa. The models effectively represent the main trends in nanoindentation results, within the experimental accuracy of the experimental values and intrinsic errors related to porosity and total organic carbon (TOC) measurements. Capturing the scaling between indentation results (modulus and hardness) and clay packing density through attributing the effect of maturity on measureable properties to different textures, established that the level of maturity, meso-scale porosity, and organic matter content control the mechanics of clay-rich phases in organic-rich shales. Given, the very low porosity of organic-rich shales (compared to other sedimentary rocks), the role of maturity and organic matter content are recognized to become more prominent for the poromechanics behavior of source rocks.

4.2. Comparison with Computational and Experimental Results

A further first-order validation consists in comparing our results obtained with the micromechanical models to the mechanical properties of illite obtained from molecular dynamics simulation. Hantal et al. [2014] obtained components of stiffness tensor of illite considering ClayFF and ReaxFF potentials. For this comparison, indentation moduli are computed from the components of the stiffness tensor for a transverse isotropic medium using equations (9) and (10). In this study, we compare indentation modulus in X3 directions, since in X1 direction nanoindentation measures the elastic stiffness as a result of the sliding of finite clay layers against each other and not the elastic stiffness of clay layers.

The resultant indentation modulus in X3 direction are 39 GPa and 39.8 GPa considering ClayFF and ReaxFF potentials, respectively. These results are in agreement with the reported value in Section 3 for the solid modulus in X3 direction (m_3=48.5 ±9.2 GPa).

The hydration state of the clay minerals may also play an important role in the mechanical properties. In fact, Ebrahimi et al. [2012] reported a value of 31 ± 7 GPa for indentation moduli in X3 direction of dry Wyoming Na-montmorillonite (basal spacing ≈ 9 Å) obtained from molecular simulations, and showed a decreasing trend in mechanical properties as basal layer spacing increases.

Bobko and Ulm [2008] performed a series of nanoindentation tests on organic-free shale samples (caprocks) containing mostly illite, smectite, and kaolinite. They reported solid phase indentation moduli, M_3=16 GPa and M_1=25 GPa. Zhang et al. [2009] also reported M_3=19.5 ± 4.9 GPa for rectonite, obtained by nanoindentation. However, it should be noted that relative humidity or basal layer spacing for the reported clay minerals is not controlled or measured during the tests. Considering the very low clay-bound water in the studied organic-rich samples compared to caprocks (36), the higher values obtained in this study are a priori expected. In case of organic-rich shales, back-analysis by Monfared and Ulm [2016] using acoustic data have resulted in m_1=62.3 GPa and m_3= 29.2, which are in close agreement with our reported values.

5. Conclusion

The combination of novel experimental and theoretical microporomechanics approaches permits advancing efforts in decoding the complex mechanical responses of organic-rich shales. By combining experimental chemomechanical characterization with advanced micromechanical modeling of the

clay/kerogen composite phases, the role of organic maturity was successfully isolated and attributed, by means of hypothesis testing, to the texture of the indented material. Thus, in a first approach, we suggest a matrix-inclusion morphology for immature samples, and a granular morphology for mature samples; while noting that "real" organic-rich source rocks are always situated in between.

In favor of our texture analysis is the obtained result for different organic-rich shale samples with clay particles exhibiting consistent and unique mechanical signature values; independent of maturity level of shale formations and total organic content (TOC). The elasticity values so obtained are in good agreement with the results obtained for illite by molecular simulation. Moreover, the developed micromechanical models show a good predictive capability in estimating volume fraction of organic matter from indentation data. Attributing the effect of different thermal maturity to a different mechanically-effective texture of the material, proposed micromechanics models of porous clay/kerogen composite, consisting of self-consistent model for mature samples and matrix-inclusion for immature samples, capture well the trend of nanoindentation results as a function of clay packing density. The above-mentioned information learned at the fundamental scales of organic-rich shales can be used for the design and validation of predictive upscaling models.

Finally, a statistical analysis performed to determine the error introduced when estimating the solid properties of clay minerals based on the back-analysis of indentation data (M and H) from individual indentation grids, suggests the need for at least 500 (at least 3 grids) independent indentation tests in the clay matrix to capture its heterogeneity and to have less than 10% of errors when calculating the clay solid properties. Errors of up to 15% should be expected when back-analyzing individual grids consisting of 100~200 indents in the clay phase.

5. Acknowledgment

This work was conducted as part of the X-Shale project, an industry-academia partnership between MIT, Shell and Schlumberger enabled through MIT's Energy Initiative. Shell and Schlumberger provided all the samples used in this study. The experimental results were obtained in the X-Hub lab at MIT: https://cshub.mit.edu.

References

1. Abedi, S., Slim, M., Hofmann, R., Bryndzia, T., Ulm, F.-J. (2016) "Nano-Chemomechanical Signature of Organic-Rich Shales: A Coupled Indentation-EDX Analysis." Acta Geotechnica, *in press*.

2. Beneviste, Y. (1987). "A New Approach to the application of Mori-Tanaka's Theory in Composite Materials." Mechanics of Materials, Vol. 6, 147-157, doi:10.1016/0167-6636(87)90005-6

3. Bobko, C. P. (2008) "Assessing the mechanical microstructure of shale by nanoindentation: The Link between mineral composition and mechanical properties." PhD dissertation, Massachusetts Institute of Technology, Cambridge.

4. Cariou, S., Ulm, F.-J., Dormieu, L. (2008) "Hardness–packing density scaling relations for cohesive-frictional porous materials" Journal of the Mechanics and Physics of Solids, Vol. 56, 924–952, doi: 10.1016/j.jmps.2007.06.011

5. Delafargue, A., Ulm, F.-J. (2004) “Explicit approximations of the indentation modulus of elastically orthotropic solids for conical indenters” International Journal of Solids and Structures, Vol. 41: 7351–7360, doi:10.1016/j.ijsolstr.2004.06.019

6. Dormieux, L., Chateau, X. (2002) “Micromechanics of saturated and unsaturated porous media” International Journal for Numerical and Analytical Methods in Geomechanics. Vol. 26(8): 831-844, doi: 10.1002/nag.227

7. Dormieux, L., Kondo, D., & Ulm, F.-J. (2006) “Microporomechanics” Chichester UK: J. Wiley & Sons. doi: 10.1002/0470032006

8. Dormieux, L., Molinari, A., Kondo, D. (2002) “Micromechanical approach to the behavior of poroelastic materials” Journal of the Mechanical and Physics of Solids. Vol. 50(10): 2203–2231, doi: 10.1016/S0022-5096(02)00008-X

9. Ebrahimi, D., Pellenq, R.J.-M., Whittle, A.J. (2012) “Nanoscale Elastic Properties of Montmorillonite Upon Water Adsorption.” Langmuir, Vol. 28(49): 16855-16863

10. Espitalié, J., Laporte, J. L., Madec, M., Marquis, F., Leplat, P., Paulet, J., and Boutefeu, A. (1977) “Méthode rapide de caractérization des roches mères, de leur potential pétrolier et de leur degré d’évolution.” Revue de L’Institut Français du Pétrole, Vol. 32, No. 1, p. 23-42, doi: 10.2516/ogst:1977002

11. Fritsch, A., Dormieux, L., Hellmich, C. Sanahuja, J. (2007) “Micromechanics of crystal interfaces in polycrystalline solid phases of porous media: fundamentals and application to strength of hydroxyapatite biomaterials” Journal of Material Science, vol. 42: 8824-8837, doi: 10.1007/s10853-007-1859-4

12. Gathier, B. (2008) “Multiscale strength homogenization: application to shale nanoindentation” S. M. dissertation, Massachusetts Institute of Technology, Cambridge.

13. Hantal, G., Brochard, L., Laubie, H., Ebrahimi, D., Pellenq, R., Ulm, F.-J., Coasne, B. (2014) “Atomic-scale modelling of elastic and failure properties of clays” Molecular Physics, Vol. 112(9-10). doi: 10.1080/00268976.2014.897393

14. Hellmich, C., Barthelemy, J-F., Dormieux, L. (2004) “Mineral–collagen interactions in elasticity of bone ultrastructure – a continuum micromechanics approach” European Journal of Mechanics - A/Solids, Vol. 23 (5): 783-810, doi: 10.1016/j.euromechsol.2004.05.004

15. Monfared, S., Ulm, F-J. (2016) “A molecular informed poroelastic model for organic-rich, naturally occurring porous geocomposites” Journal of the Mechanics and Physics of Solids, in press.

16. Mori, T., Tanaka, K. (1973). “Average stress in matrix and average elastic energy of materials with misfitting inclusions”. Acta Metallurgic, Vol. 21, Issue 5, 571-574, doi: 10.1016/0001-6160(73)90064-3
Ortega, J. A., Ulm, F.-J., Abousleiman, Y. (2009) “The nanogranular acoustic signature of shale“ Geophysics, Vol. 74 (3): D65-D84, doi: 10.1190/1.3097887

17. Ortega, J.A., Ulm, F.-J., Abousleiman, Y. (2009). “The nanogranular acoustic signature of shale.”

Geophysics, Vol 74 (3): 65-84

18. Prasad, M., Mukerji, T., Reinstaedler, M., Arnold, W. (2009a) "Acoustic Signatures, Impedance Microstructure, Textural Scales, and Anisotropy of Kerogen-Rich Shales" SPE Annual Technical Conference and Exhibition, 4-7 October, New Orleans, Louisiana, doi: 10.2118/124840-MS

19. Prasad, M., Mba, K. C., McEvoy, E., and Batzle, M. L. (2009b) "Maturity and impedance analysis of organic-rich shales. Society of Petroleum Engineers." SPE 123531; doi:10.2118/123531-MS

20. Prasad, M., Mukerji, T. (2003) "Analysis of Microstructural Textures And Wave Propagation Characteristics In Shales" SEG Annual Meeting, 26-31 October, Dallas, Texas.

21. Ulm, F.-J., Vandamme, M., Bobko, C., Ortega., J. A. (2007) "Statistical Indentation Techniques for Hydrated Nanocomposites: Concrete, Bone, and Shale" Journal of the American Ceramic Society, Vol. 90 (9): 2677-2692, doi: 10.1111/j.1551-2916.2007.02012.x

22. Zaoui, A. (2002). "Contiuum Micromechanics: A Survey" Journal of Engineering Mechanics, Vol. 128, 808-816, doi: 10.1061/(ASCE)0733-9399(2002)128:8(808)

23. Zargari, S., Prasad, M., Mba, K. C., and Mattson, E. D. (2013) "Organic maturity, elastic properties, and textural characteristics of self resourcing reservoirs." Geophysics, Vol. 78, No. 4, P. D223-D235, doi:10.1190/GEO2012-0431.1

24. Gayer, J., Prasad, M., Batzle, M. (2015) "Comparison of anhydrous to hydrous pyrolysis effects on oil shale core samples from the Iratì Formation in the Paraná Basin, Brazil" SEG Annual Meeting, 18-23 October, New Orleans, Louisiana

25. Allan, AM., Clark, AC., Vanorio, T. (2015) "Pyrolysis-Induced Evolution of the Elastic and Transport Properties of the Barnett Shale." SEG Annual Meeting, 18-23 October, New Orleans, Louisiana

26. Okiongbo, KR., Aplin, AC., and Larter, SR. (2005) "Changes in type II kerogen density as a function of maturity: Evidence from the Kimmeridge Clay Formation." Energy Fuels, Vol 19(6): 2495 – 2499.

27. Mavko, G., Mukerji, T., Dvorkin, J.(2009). "Rock Physics Handbook: Tools for Seismic Analysis in Porous media" Cambridge University Press.

28. Vernik, L., Landis, C. (1996). "Elastic anisotropy of source rocks: Implications for hydrocarbon generation and primary migration" AAPG Bulletin, Vol. 80(4): 531– 544

29. Chen, J. J., Sorelli, L., Vandamme, M., Ulm, F-J., Chanvillard, G. (2010) "A coupled nanoindentation/SEM-EDS study on low water/cement ratio portland cement paste: evidence for C–S–H/Ca(OH)2 nanocomposites" Journal of American Ceramic Society, Vol. 93(5): 1484-1493, doi: 10.1111/j.1551-2916.2009.03599.x

30. Deirieh, A., Ortega, J. A., Ulm, F.-J., and Abousleiman, Y. (2012) "Nanochemomechanical assessment of shale: a coupled WDS-indentation analysis" Acta Geotechnica, 7, 271-295, doi: 10.1007/s11440-012-0185-4

31. Ulm, F-J., Vandamme, M., Bobko, C. P., Ortega, J. A., Tai, K., Ortiz, C. (2007) "Statistical Indentation Techniques for Hydrated Nanocomposites: Concrete, Bone, and Shale. " Journal of American Ceramic Society Vol. 90(9): 2677-2692, doi:10.1111/j.1551-2916.2007.02012.x

32. Vernik, L., Kachanov, M. (2010) "Modeling elastic properties of siliciclastic rocks" Geophysics, Vol. 75 (6): E171–E182.

33. Vernik, L., and Nur, A. (1992) "Ultrasonic velocity and anisotropy of hydrocar- bon source rocks" Geophysics, Vol. 57: 727–735.

34. Kuila, U., McCarty, DK., Derkowski, A., Fischer, TB., Topór, T., Prasad, M. (2014) "Nano-scale texture and porosity of organic matter and clay minerals in organic-rich mudrocks." Fuel Vol. 135: 359–373, doi:10.1016/j.fuel.2014.06.036

35. Fitzgerald, JJ., Hamza, AI., Bronnimann, CE., Dec, SF. (1989) "Solid-state 27 Al and 29 Si NMR studies of the reactivity of the aluminum-containing clay mineral kaolinite" Solid State Ionics, Vol. 32–33, Part 1: 378-388

36. Sone, H., Zoback, MD. (2013) "Mechanical properties of shale gas reservoir rocks — Part 1: Static and dynamic elastic properties and anisotropy." Geophysics, 78, doi: 10.1190/geo2013-0050.1.

Figures:

Figure 1. Multiscale thought-model of organic-rich shale. Level 0 corresponds to the scale of elementary clay particles at nanometer length scales. Level I is a porous clay/kerogen composite at the scale of micrometer (scale of indentation), with the porosity representing the mesoporosity. Level II is the scale of porous organic/inorganic hard inclusion composite.

Figure 2. Conical indentation in a porous organic/inorganic composite (modified from [4](a) granular (self-consistent) morphology used to represent the texture of mature samples and (b) matrix-inclusion (Mori-Tanaka) morphology used for immature samples. The characteristic voxel size in an indentation test using Berkovich indenter corresponds approximately to 3- 5 times the indentation depth (Constantinides and Ulm, 2007). With an average maximum indentation depth, $h_{max} = 400 - 800$ nm for the indentation tests performed in this study, the average material domain inquired by the Berkovich indenter is on the order of 1-4 μm.

Figure 3. Normalized indentation modulus as a function of solid (inorganic + organic) packing density for a (a) granular morphology and (b) matrix-inclusion morphology. The blue curve represents the normalized homogenized response of the material composed of an inorganic solid phase and pore space. The orange dashed line displays the response of the porous organic/inorganic composite.

Figure 4. Normalized indentation hardness as a function of solid (inorganic + organic) packing density for a (a) granular morphology and (b) matrix-inclusion morphology. The blue curve represents the normalized homogenized response of the material composed of an inorganic solid phase and pore space. The orange dashed line displays the response of the porous organic/inorganic composite.

Figure 5. Typical plots of indentation modulus and hardness versus local solid packing density at each individual indentation point [Haynesville].

Figure 6. a) Normalized mean values of solid properties and packing density and b) error window ($\mu \pm \sigma$) expected at different sample size. Note the large standard deviations or error intervals seen with small sample sizes (n<500). (etak = η_k)

Figure 7. Clay indentation modulus obtained from back-analysis of indentation results of all samples versus (a) volume fraction of kerogen and (b) volume fraction of clay. The shaded areas represent the range of values obtained for clay indentation modulus in X1 and X3 directions.

Figure 8. Clay hardness obtained from backanalysis of indentation results of all samples versus (a) volume fraction of kerogen and (b) clay packing density. The shaded areas represent the range of values obtained for clay hardness in X1 and X3.

Figure 9. Volume fraction of kerogen predicted by the model versus the values obtained from experimental TOC measurements.

Figure 10. Indentation modulus of clay-rich phases of all investigated samples as a function of clay packing density ($\eta_c = 1 - \eta_k - \varphi^I$). Bold curves represent model curves in X1 direction (MT for Mori-Tanaka and SC for Self-Consistnt morphology) and regular ones are corresponding curves in X3 direction.

Figure 11. Indentation hardness of clay-rich phases of all investigated samples as a function of clay packing density ($\eta_c = 1 - \eta_k - \varphi^I$). Bold curves represent model curves (MT for Mori-Tanaka and SC for Self-Consistent morphology) and regular ones are corresponding curves in X3 direction.

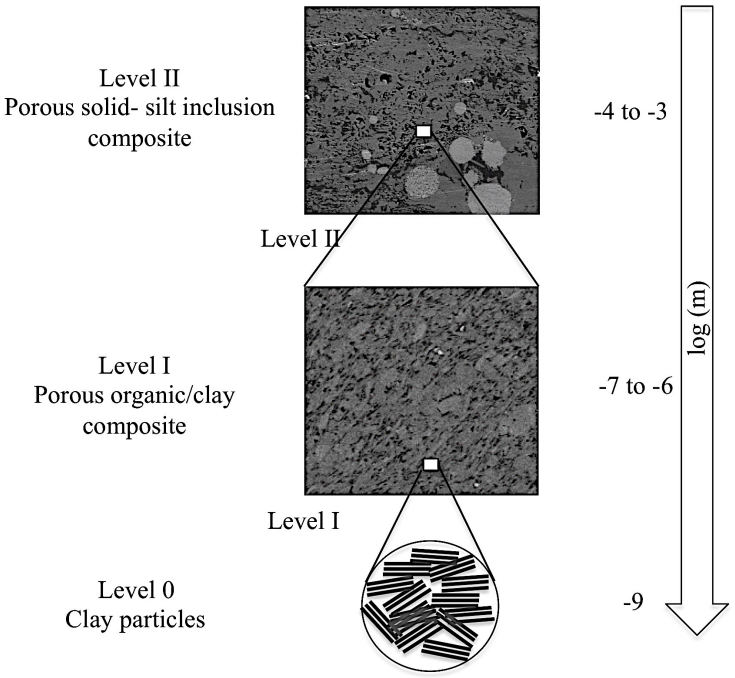

Figure 1. Multiscale thought-model of organic-rich shale. Level 0 corresponds to the scale of elementary clay particles at nanometer length scales. Level I is a porous clay/kerogen composite at the scale of micrometer (scale of indentation), with the porosity representing the mesoporosity. Level II is the scale of porous organic/inorganic hard inclusion composite [Abedi et al., 2016]

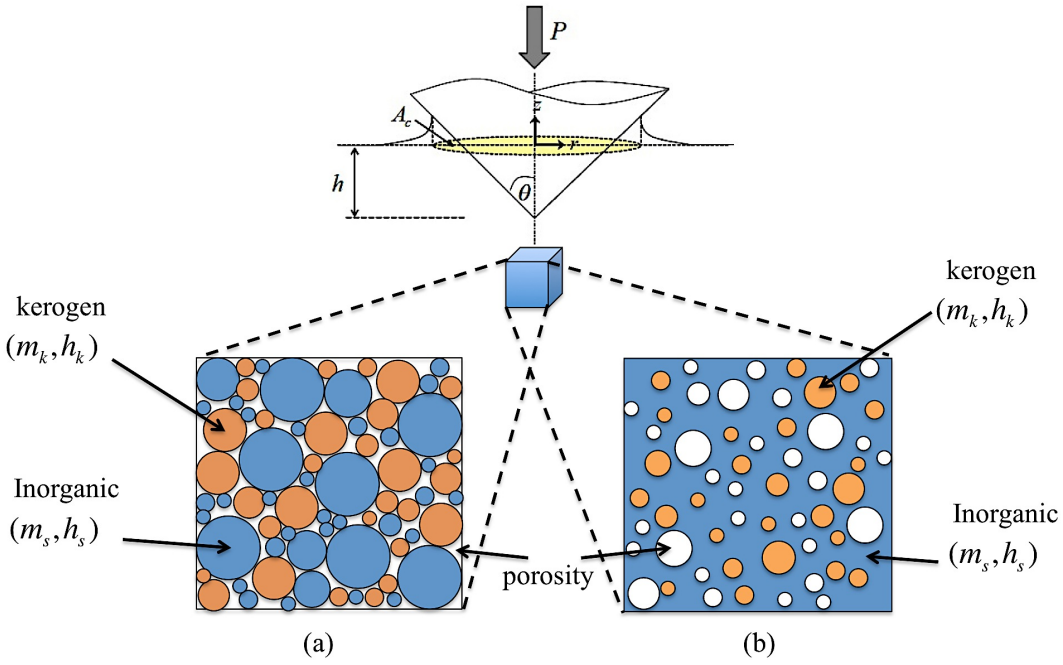

Figure 2. Conical indentation in a porous organic/inorganic composite (modified from [4]): (a) granular (self-consistent) morphology used to represent the texture of mature samples and (b) matrix-inclusion (Mori-Tanaka) morphology used for immature samples. The characteristic voxel size in an indentation test using Berkovich indenter corresponds approximately to 3- 5 times the indentation depth (Constantinides and Ulm, 2007). With an average maximum indentation depth, $h_{max} = 400 - 800$ nm for the indentation tests performed in this study, the average material domain inquired by the Berkovich indenter is on the order of 1-4 μm.

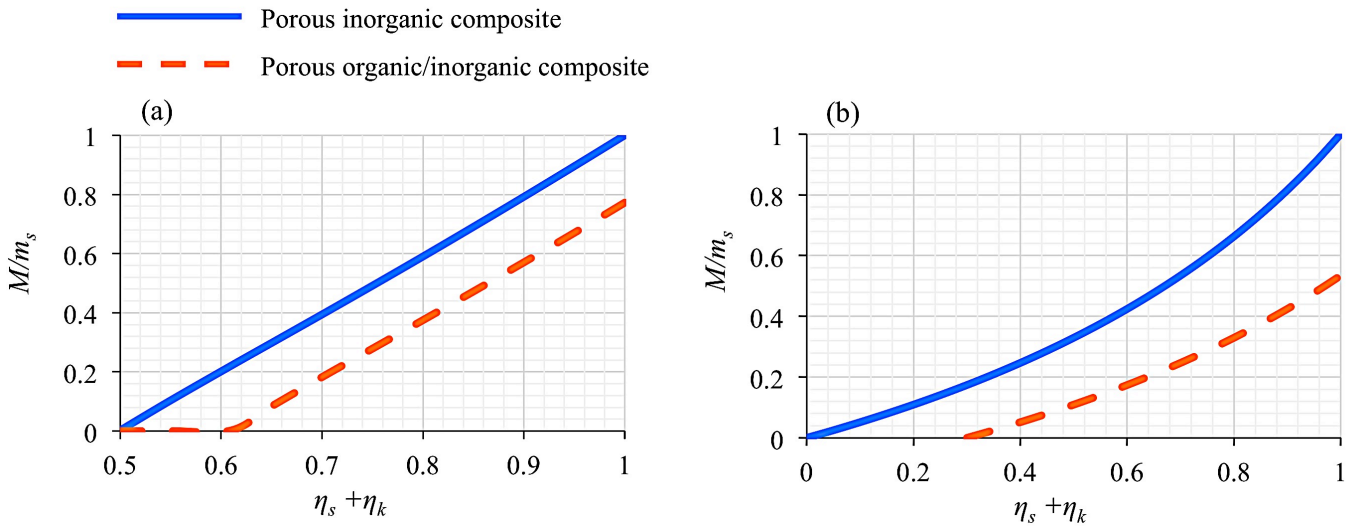

Figure 3. Normalized indentation modulus as a function of solid (inorganic + organic) packing density for a (a) granular morphology and (b) matrix-inclusion morphology. The blue curve represents the normalized homogenized response of the material composed of an inorganic solid phase and pore space. The orange dashed line displays the response of the porous organic/inorganic composite.

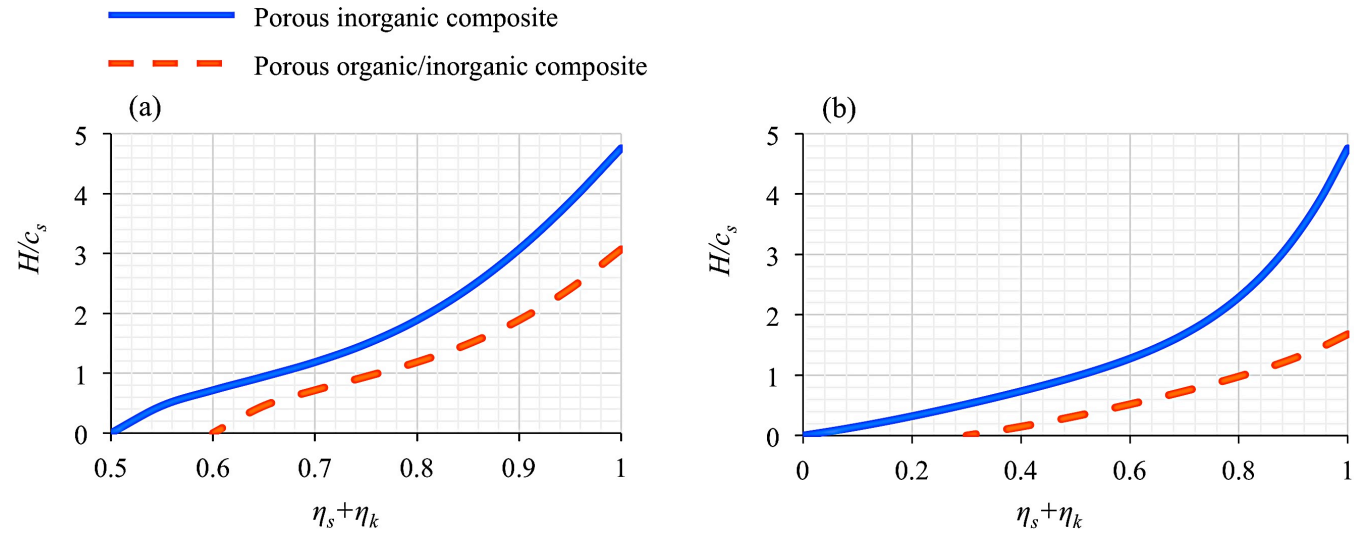

Figure 4. Normalized indentation hardness as a function of solid (inorganic + organic) packing density for a (a) granular morphology and (b) matrix-inclusion morphology. The blue curve represents the normalized homogenized response of the material composed of an inorganic solid phase and pore space. The orange dashed line displays the response of the porous organic/inorganic composite.

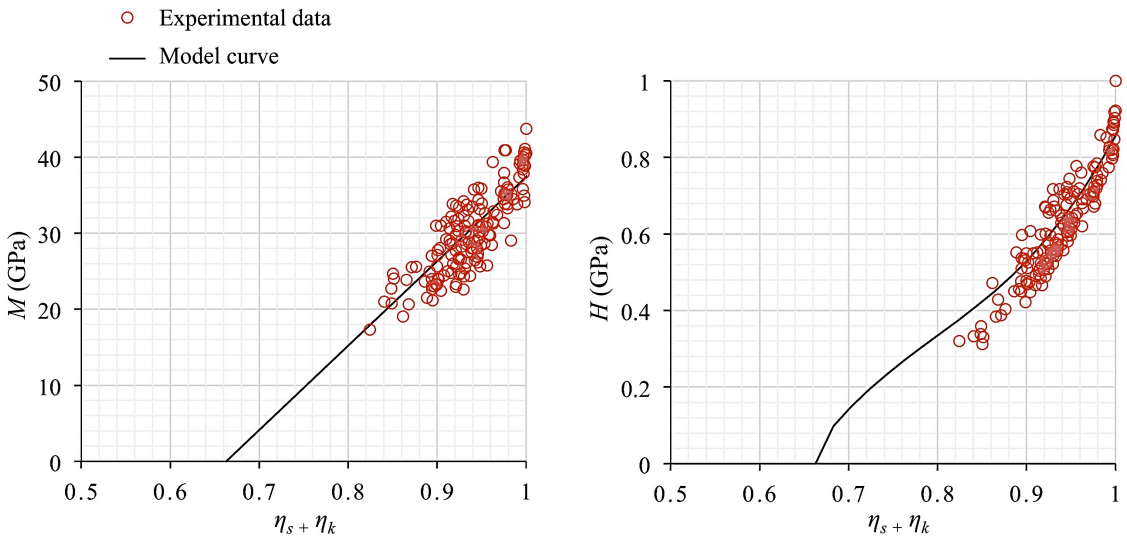

Figure 5. Typical plots of indentation modulus and hardness versus local solid packing density at each individual indentation point [Haynesville]. The continuous line represents model curve and

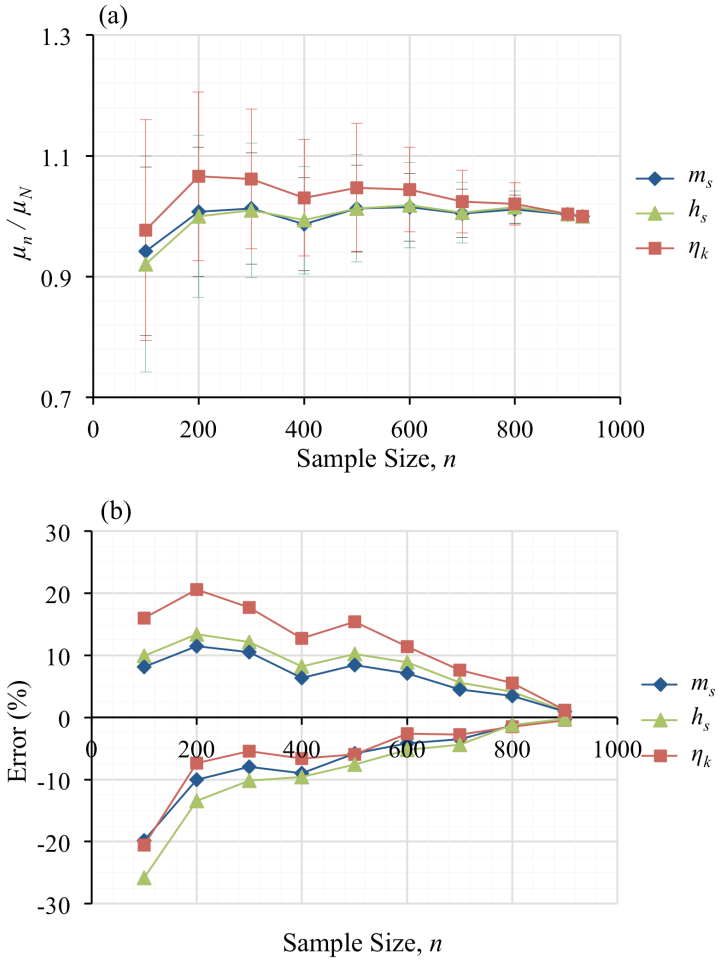

Figure 6. a) Normalized mean values of solid properties and packing density and b) error window ($\mu \pm \sigma$) expected at different sample size. Note the large standard deviations or error intervals seen with small sample sizes (n<500). (etak = η_k)

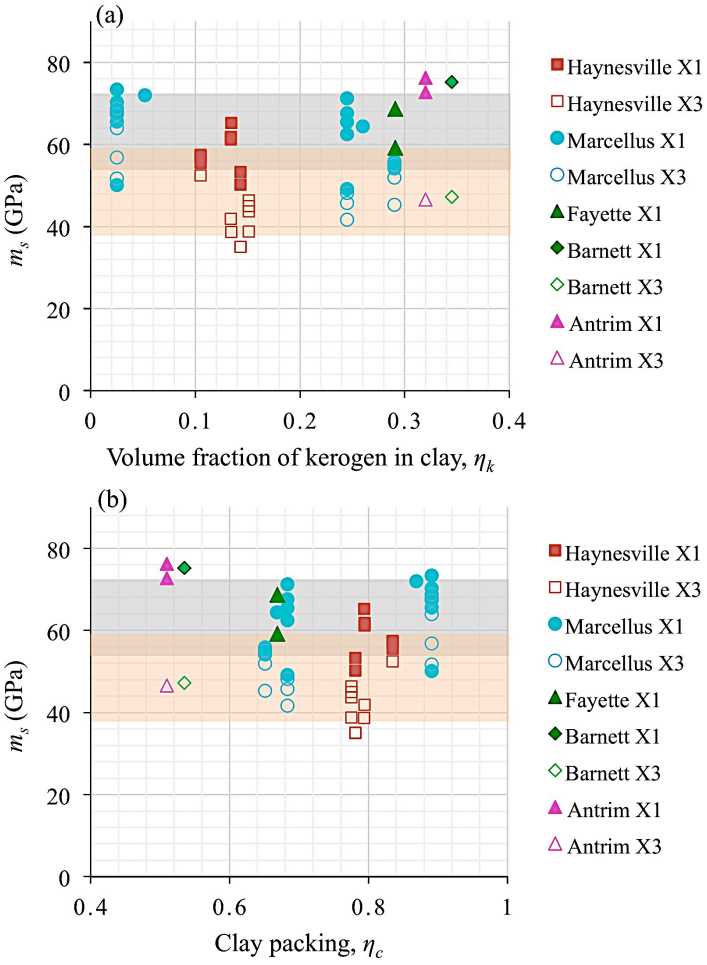

Figure 7. Clay indentation modulus obtained from back-analysis of indentation results of all samples versus (a) volume fraction of kerogen and (b) volume fraction of clay. The shaded areas represent the range of values obtained for clay indentation modulus in X1 and X3 directions.

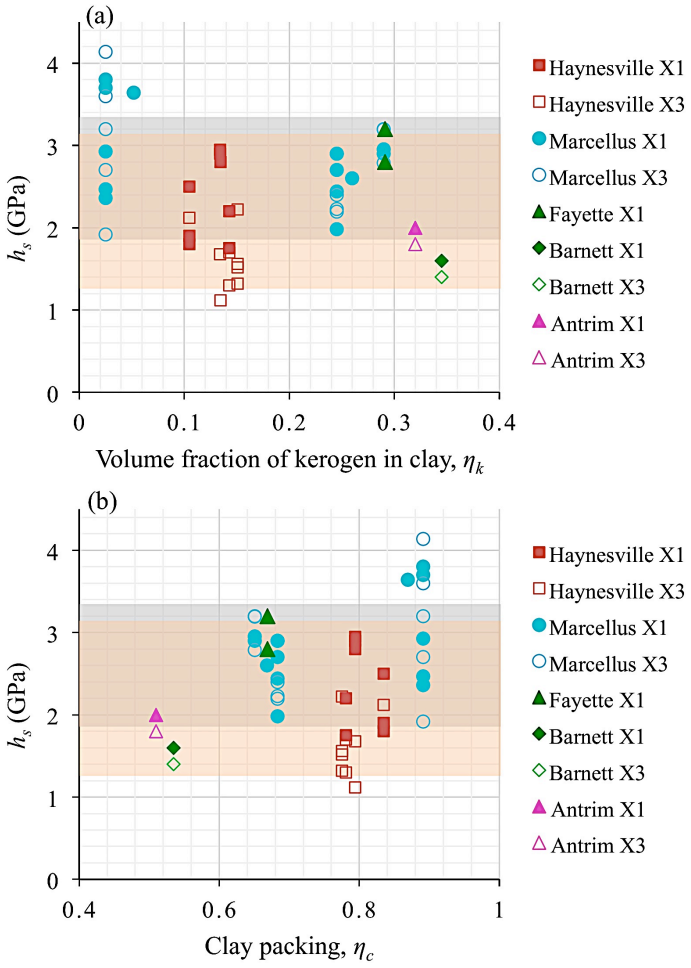

Figure 8. Clay hardness obtained from back-analysis of indentation results of all samples versus (a) volume fraction of kerogen and (b) clay packing density. The shaded areas represent the range of values obtained for clay hardness in X1 and X3.

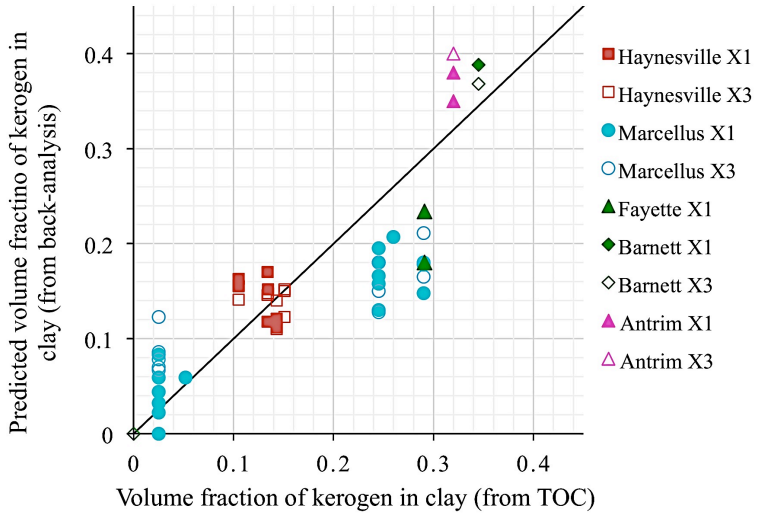

Figure 9. Volume fraction of kerogen predicted by the model versus the values obtained from experimental TOC measurements.

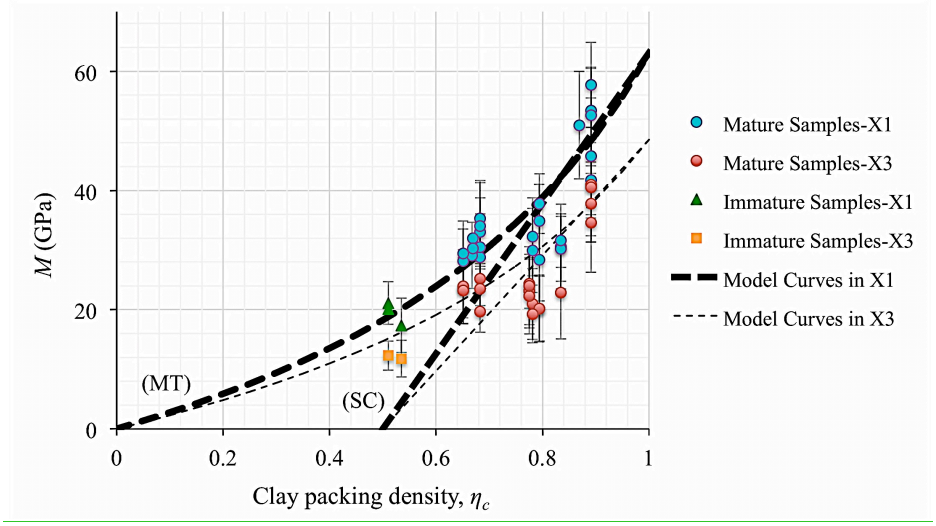

Figure 10. Indentation modulus of clay-rich phases of all investigated samples as a function of clay packing density ($\eta_c = 1 - \eta_k - \varphi^I$). Bold curves represent model curves in X1 direction (MT for Mori-Tanaka and SC for Self-Consistent morphology) and regular ones are corresponding curves in X3 direction.

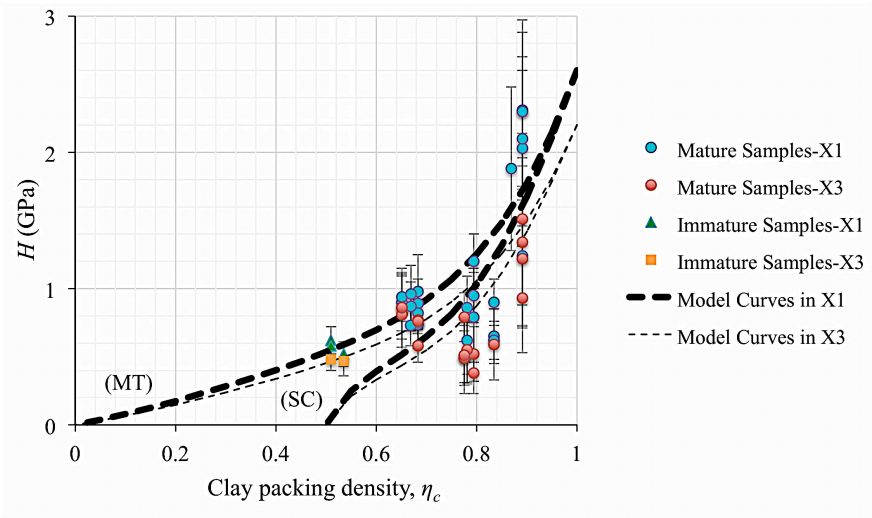

Figure 11. Indentation hardness of clay-rich phases of all investigated samples as a function of clay packing density ($\eta_c = 1 - \eta_k - \varphi^I$). Bold curves represent model curves (MT for Mori-Tanaka and SC for Self-Consistent morphology) and regular ones are corresponding curves in X3 direction.

Table 1. Mineralogy, porosity and TOC measurements of the studied samples[a]

Sample group	Clay (wt. %)	Quartz (wt. %)	Carbonates (wt. %)	TOC (wt. %)	Porosity (%)
Haynesville	38-45	27-32	9-22	2.6-3.3	6-7.6
Marcellus1	38.9-39.9	18.7-19.7	35.5-37	0.5-1	7.9-8.4
Marcellus2	41.2-48.6	29.4-36.2	4.8-16.1	7.32-8.18	5.9-7.2
Fayetteville	25.1	28.8	31.7	4.9	4
Barnett	41.8	29.7	2.6	12.2	7.3
Antrim	31.41	40.9	4.4	9.6	8.8

[a]The mineralogy data were obtained by x-ray diffraction (XRD; courtesy of Shell).

Table 2. Volume fraction of different material phases present in the studied samples.

Sample group	Clay (vol.%)	Quartz (vol.%)	Carbonates (vol.%)	Kerogen (vol.%)
Haynesville	33.1-39.9	23.5-28.1	7.7-18.7	5-6.4
Marcellus1	35.4-36.5	17.3-18.4	32-33.1	1-2.1
Marcellus2	34.1-40.1	24.8-30.4	3.8-13.1	13.6-15.2
Fayetteville	22.7	26.1	27.6	9.85
Barnett	33.4	23.9	2.1	21.4
Antrim	24.5	34.4	3.4	16

Table 3. Volume fraction of kerogen at level I for the studied samples.

Sample	Haynesville	Marcellus-1	Marcellus-2	Fayetteville	Barnett	Antrim
η_k	10.5-15	2.5-5.2	24.3-28.8	29.1	34.4	32

Table 4. Porosity at level I for Barnett and Antrim samples.

	Barnett	Antrim
φ^I	12	17

View publication stats